Clustering and spatial distribution of mitochondria in dendritic trees

M. Hidalgo-Soria and E. F. Koslover*
Department of Physics, University of California, San Diego, La Jolla, California 92093, USA

(Received 7 May 2024; accepted 27 November 2024; published 24 December 2024)

Neuronal dendrites form densely branched tree architectures through which mitochondria must be distributed to supply the cell's energetic needs. Dendritic mitochondria circulate across the tree, undergoing fusion and fission to form clusters of varying sizes. We present a mathematical model for the distribution of such actively driven interacting particles in a branched geometry, showing that the density and localization of particles is highly sensitive to the fusion/fission balance and to the tree architecture. Our model demonstrates that "balanced" trees (wherein cross-sectional area is conserved across junctions and thicker branches support more bushy subtrees) enable symmetric yet distally enriched particle distributions and promote dispersion into smaller clusters. These results highlight the importance of tree morphology and radius-dependent fusion in governing the distribution of neuronal mitochondria.

DOI: 10.1103/PhysRevResearch.6.043312

I. INTRODUCTION

Extended neuronal cells face the challenging task of spatially distributing organelles such as mitochondria, which provide a source of energy for neuronal function. Mitochondrial structures range from highly interconnected architectures in yeast cells [1], to largely fragmented populations in axons [2,3], to networks on the border of percolation in many mammalian cell types [4–6]. In dendrites, mitochondria circulate through the cell, forming a "social" network of variable-size clusters whose dynamic fusion and fission are thought to maintain homeostasis by helping deliver newly synthesized material from the soma [7–9].

Live-cell imaging of dendritic mitochondria in *Drosophila* sensory HS neurons has revealed a mixed population of stationary disjoint clusters and small motile mitochondria that move processively in anterograde or retrograde directions [10]. The dendritic arbors themselves form a bifurcating tree rooted at the cell body, with narrowing branches towards the distal tips [Fig. 1(a)]. The steady-state distribution of mitochondria was found to exhibit two robust features: enrichment of mitochondrial volume density towards the distal tips and symmetric volume densities between sister subtrees [10].

The spatial distribution of mitochondria modulates gradients in ATP availability and metabolic efficiency [11,12], particularly in highly extended neuronal geometries. Defects in mitochondrial transport, localization, and interaction are associated with a number of neuropathologies, including Alzheimer's and Parkinson's disease [13–15]. Consequently, the mechanisms by which neurons control and establish mitochondrial localization constitute an important problem in cellular neuroscience. While mitochondrial localization in some cell types is governed by glucose concentrations [16], calcium levels [17], or local neuronal activity [18,19], the distributions observed in *Drosophila* sensory dendrites were found to be insensitive to such signals [10]. Instead, the distributions appeared to be maintained autonomously as a dynamic steady state of the mitochondrial population, which turns over on a few-hour timescale.

In past work we developed a simple theoretical model for mitochondrial distribution in a branched tree structure that incorporated bidirectionally moving mitochondrial units which halt their transport with a radius-dependent rate constant [10]. It was shown that the observed spatial distributions could only be obtained if the architecture of the dendritic trees approximately followed specific scaling laws. Morphological measurements of the arbors showed that HS neuron dendrites do in fact exhibit the predicted scaling. Namely, branch widths obey the da Vinci law [20], which preserves cross-sectional area across a junction ($r_0^2 = r_1^2 + r_2^2$, where r_0 is the radius of the parent branch and r_1, r_2 the radii of the two daughter branches). In addition, sister branch radii have areas in proportion to the "bushiness" of the corresponding subtrees (B_i, total branch length over depth), such that $r_1^2/r_2^2 = B_1/B_2$. Hereafter, we refer to architectures that obey these two scaling laws as "balanced trees."

Crucially, the basic model in Ref. [10] did not account for the fusion of mitochondria into variable-size clusters. Fusion of mitochondria into extended structures is thought to protect against cellular stress [21,22] and modulate ATP production [23]. Furthermore, fusion and fission dynamics have been hypothesized to play an important role in mitochondrial quality control [24,25] and to allow for complementation of mitochondrial DNA [26,27]. Alterations in the balance of fusion and fission have been shown to directly regulate the architecture of mitochondrial networks, both in mathematical

*Contact author: ekoslover@ucsd.edu

modeling studies [5,6] and in live cells [1,5]. Because bigger clusters tend to be immobile [28], the fusion of dendritic mitochondria into clusters must couple together with their distribution throughout the arbor. In this work, we develop a model that incorporates mitochondrial fusion and fission to explore the interplay of cluster formation and spatial localization of mitochondria in treelike domains.

The fusion of mitochondria into larger clusters is analogous to reversible aggregation and polymerization phenomena, previously explored in the context of pathogenic protein aggregates [29], filaments [30], and gels [31]. Such systems have traditionally been studied via kinetic mass-action models [32–36], which generally assume that fusion, fission, absorption, and injection of particles occur in an unstructured homogeneous space and that the system can be treated as well mixed. Here we consider how the spatial architectures of dendritic arbors, as well as active transport and geometry-dependent fusion, modulate the formation of mitochondrial clusters.

We develop a spatially resolved mass-action model for the distribution of actively driven clustering particles (representing mitochondria) on binary trees (representing *Drosophila* sensory dendrites). We demonstrate that balanced tree architectures can give rise to a universal cluster distribution that is independent of the specific branching pattern. Furthermore, such structures are shown to allow for the broadest dispersion of particles into the smallest possible clusters. Our model links together mitochondrial fusion and spatial localization, thereby shedding light on the interconnection of regulatory pathways that have previously been shown to modulate each one of these processes individually.

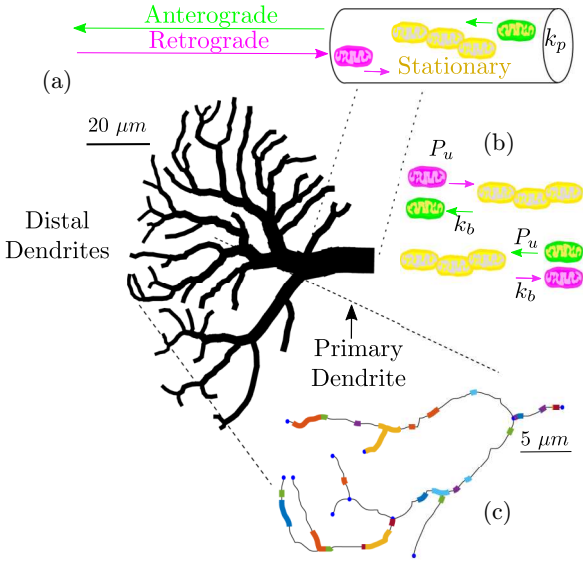

FIG. 1. Model schematic. (a) Skeleton of a dendritic tree topology extracted from *Drosophila* HS neurons [10], with branch radii set to obey a balanced tree morphology. Inset: Schematic of anterograde (green), retrograde (magenta), and stationary (yellow) mitochondria at the primary trunk. Anterograde mitochondria are produced at rate k_p. (b) Fusion and fission dynamics in the mitochondrial cluster model. Fusion occurs with probability P_u during each passage event; fission at each cluster end occurs at constant rate k_b. (c) Simulation snapshot of mitochondrial clusters with different sizes on dendritic branches; different colors indicate distinct mitochondrial clusters.

II. MODEL DEVELOPMENT

In this work we introduce a model for dendritic mitochondria distribution that incorporates fusion and fission of mitochondria into stationary clusters, processive transport of mitochondrial units, and a branching geometry for the dendritic arbor. The primary aim of this model is to explore the link between the mitochondrial network structure (i.e., cluster sizes) and its spatial distribution. While we follow an analogous approach to prior work [10], the introduction of mitochondrial fusion into clusters makes this model fundamentally distinct.

The dendritic arbor is represented as a bifurcating tree rooted at the cell body, with narrowing branches towards the distal tips [Fig. 1(a)]. Mitochondria are modeled as a population of discrete units that engage in transport, fission, and fusion [Fig. 1(b)]. Single motile units move processively with velocity $\pm v$ (anterograde or retrograde) and reverse at distal branch tips. New mitochondria are produced at the soma (tree root) with rate k_p. Retrograde mitochondria that return to the root disappear. When a motile mitochondrion passes the tip of any mitochondrial cluster, it has a probability of fusion: $P_{u,j} = A_u/r_j^\gamma$, with r_j the radius of the branch j, γ a scaling exponent that governs sensitivity to branch width, and A_u a prefactor setting the overall tendency towards fusion. We assume that all stops or arrests of motile mitochondria are due to fusion with stationary clusters. The scaling of the fusion probability with branch radius is then based on the experimental evidence that motile mitochondria tend to stop more at distal areas [10], and we explore the role of the scaling exponent γ in determining mitochondrial distributions. Fused clusters are assumed to be always stationary, a simplified reflection of the observation that larger mitochondria in dendritic process are less likely to be motile [28].

Clusters can undergo fission with rate k_b at each end, releasing a single motile mitochondrial unit while the remainder of the cluster remains stationary. A stationary single unit becomes motile again also with rate k_b and is equally likely to go anterograde or retrograde. Anterograde mitochondria split at junctions in proportion to the cross-sectional area of the respective daughter branches, as observed in *Drosophila* sensory dendrites [10].

This model can be explicitly represented in agent-based simulations (see Appendix A for details), which track the motion of individual mitochondrial units and the spatial extent of growing clusters [Fig. 1(c); Supplemental video SV1 [37]]. To more efficiently explore the behavior of this dynamic system, we represent it in terms of a spatially resolved mass-action model, which treats all clusters as pointlike particles and assumes that the cluster distributions can be described in terms of continuum concentration fields. The mitochondria are represented by linear densities $\rho_{i,j}^{\omega}$ of clusters with size i located on branch j in state $\omega = \{+, -, s\}$ (corresponding to anterograde, retrograde, and stationary particles, respectively). The time evolution of the linear densities is given by the following set of equations, which incorporate all state

transitions:

$$\begin{aligned}
\frac{\partial \rho^s_{1,j}}{\partial t} &= -2k_b\rho^s_{1,j} + 2k_b\rho^s_{2,j} - vP_{u,j}(\rho^+_{1,j} + \rho^-_{1,j})\rho^s_{1,j},\\
\frac{\partial \rho^\pm_{1,j}}{\partial t} &= \mp v\frac{\partial \rho^\pm_{1,j}}{\partial x} - vP_{u,j}\rho^\pm_{1,j}\sum_{i=1}^{\infty}\rho^s_{i,j} - 2vP_{u,j}\rho^-_{1,j}\rho^+_{1,j}\\
&\quad + k_b\sum_{i=1}^{\infty}\rho^s_{i,j},\\
\frac{\partial \rho^s_{2,j}}{\partial t} &= -vP_{u,j}(\rho^+_{1,j} + \rho^-_{1,j})\rho^s_{2,j} + 2vP_{u,j}\rho^-_{1,j}\rho^+_{1,j} + 2k_b\rho^s_{3,j}\\
&\quad - 2k_b\rho^s_{2,j} + vP_{u,j}(\rho^+_{1,j} + \rho^-_{1,j})\rho^s_{1,j},\\
\frac{\partial \rho^s_{i,j}}{\partial t} &= vP_{u,j}(\rho^+_{1,j} + \rho^-_{1,j})\left(\rho^s_{i-1,j} - \rho^s_{i,j}\right) + 2k_b\rho^s_{i+1,j}\\
&\quad - 2k_b\rho^s_{i,j}, \quad \text{(for } i > 2\text{)}.
\end{aligned} \tag{1}$$

The boundary condition at the primary trunk matches the flux of anterograde mitochondria to the production rate: $v\rho^+_{1,0}(0) = k_p$. At the distal tips, we assume reflective boundary conditions, with anterograde mitochondria flipping to retrograde motion when they reach the tips, giving $\rho^+_{1,j}(\ell_j) = \rho^-_{1,j}(\ell_j)$ for any terminal branches j of length ℓ_j. At each junction between parent branch j and daughter branches k, l we set boundary conditions to match the incoming and outgoing flux in both directions: $\rho^{+/-}_{1,j}(\ell_j) = \rho^{+/-}_{1,k}(0) + \rho^{+/-}_{1,l}(0)$. Furthermore, the anterograde flux is assumed to split in proportion to the cross-sectional area of the daughter branches (as observed in live-cell measurements of dendritic mitochondrial transport [10]): $\rho^+_{1,k}(0)/\rho^+_{1,l}(0) = r_k^2/r_l^2$.

We then proceed to solve for the steady-state linear densities of all clusters throughout the branches (details in Appendix B). At steady state, the mitochondrial densities are constant on each branch and the anterograde and retrograde densities are equal ($\rho^+_{1,j} = \rho^-_{1,j}$) everywhere. For simplicity, we define the total density of motile mitochondria as $\rho^m_{1,j} = \rho^+_{1,j} + \rho^-_{1,j}$. The overall steady-state solution of Eq. (1) is given by:

$$\begin{aligned}
\rho^s_{1,j} &= \frac{1}{2}\alpha_j\left(\rho^m_{1,j}\right)^2\\
\rho^s_{i,j} &= \frac{\rho^m_{1,j}}{2}\left(1 + \alpha_j\rho^m_{1,j}\right)\left(\alpha_j\rho^m_{1,j}\right)^{i-1}; \quad i > 1,
\end{aligned} \tag{2}$$

where $\alpha_j = vA_u/2k_br_j^\gamma$, $\rho^m_{1,0} = 2k_p/v$ is the motile density at the root of the tree, and motile densities in all other branches are found by applying the junction boundary conditions. For da Vinci trees (where $r_j^\alpha = r_k^\alpha + r_l^\alpha$ with $\alpha = 2$ at each junction), this gives a simple relationship between the parent and daughter motile densities: $\rho^m_{1k} = \rho^m_{1j}(r_k^2/r_j^2)$. The linear density of motile mitochondria on each branch can then be written in closed form:

$$\rho^m_{1,j} = \frac{2k_pr_j^2}{vr_0^2}. \tag{3}$$

For trees that do not obey da Vinci scaling (e.g., $\alpha \neq 2$), the linear density of motile monomers must be computed recursively at each junction by starting with the primary trunk density and computing each successive pair of daughter branch densities as:

$$\rho^m_{1,k} = \rho^m_{1,j}\frac{r_k^2}{r_k^2 + r_l^2}; \quad \rho^m_{1,l} = \rho^m_{1,j}\frac{r_l^2}{r_k^2 + r_l^2}. \tag{4}$$

The volume density of clusters of size i in motility state ω on each branch j is defined as $c^\omega_{i,j} = \rho^\omega_{i,j}/(\pi r_j^2)$. The branch radii thus play several distinct roles in setting mitochondrial densities: They link linear and volume densities, they determine the linear density of motile mitochondria in downstream branches, and they modulate the fusion probability through the scaling exponent γ.

In order to describe the morphology of the branched tree through which mitochondria move, we define the depth of a tree or subtree in a recursive manner, as follows. For arbors where every tip has the same path length from the root, the depth D_0 is equal to this path length. For general architectures, the depth is defined as

$$D_0 = \ell_0 + \frac{L_1 + L_2}{L_1/D_1 + L_2/D_2}, \tag{5}$$

where ℓ_0 is the length of the trunk and L_j, D_j are the total branch length and the depth of the daughter subtrees. This expression averages the inverse depth of daughter subtrees, weighted by their corresponding lengths, as well as adding on the length of the parent trunk. The bushiness of a subtree is defined as the total branch length divided by the depth ($B_j = L_j/D_j$). For a balanced tree morphology, where cross-sectional area is conserved across junctions and sister branch radii are proportional to the subtree bushiness, the depth is directly related to the total tree volume according to $V_0 = \pi r_0^2 D_0$ (see Appendix C). Thus, the recurrent definition of depth used here enables an intuitive relation between tree volume, branch width, and depth to be extended to more complex branching architectures.

III. RESULTS

A. Mass-action model and agent-based simulations give matching predictions of cluster distribution

To demonstrate the utility of the mass-action model, we compare its predictions to agent-based simulations on a small tree (Fig. 2), with branch length and connectivity extracted from a portion of an HS dendritic arbor [10], and branch radii set to obey a balanced tree morphology. We compute the normalized distribution of cluster sizes (p_i) and the volume density in each branch (c_j) according to

$$p_i = \left(\sum_j \rho_{i,j}\ell_j\right)\Bigg/\left(\sum_j\sum_{i=1}^{\infty}\rho_{i,j}\ell_j\right), \tag{6}$$

$$c_j = \left(\rho^m_{1,j} + \sum_{i=1}^{\infty} i\rho^s_{i,j}\right)\Bigg/\left(\pi r_j^2\right), \tag{7}$$

where the summations over j correspond to all branches of the tree and summation over i corresponds to all cluster sizes. To place the model in a biologically relevant regime, we estimate the volume of a mitochondrial unit as $v \approx 0.5\ \mu\text{m}^3$, and select kinetic parameters such that the average mitochondrial

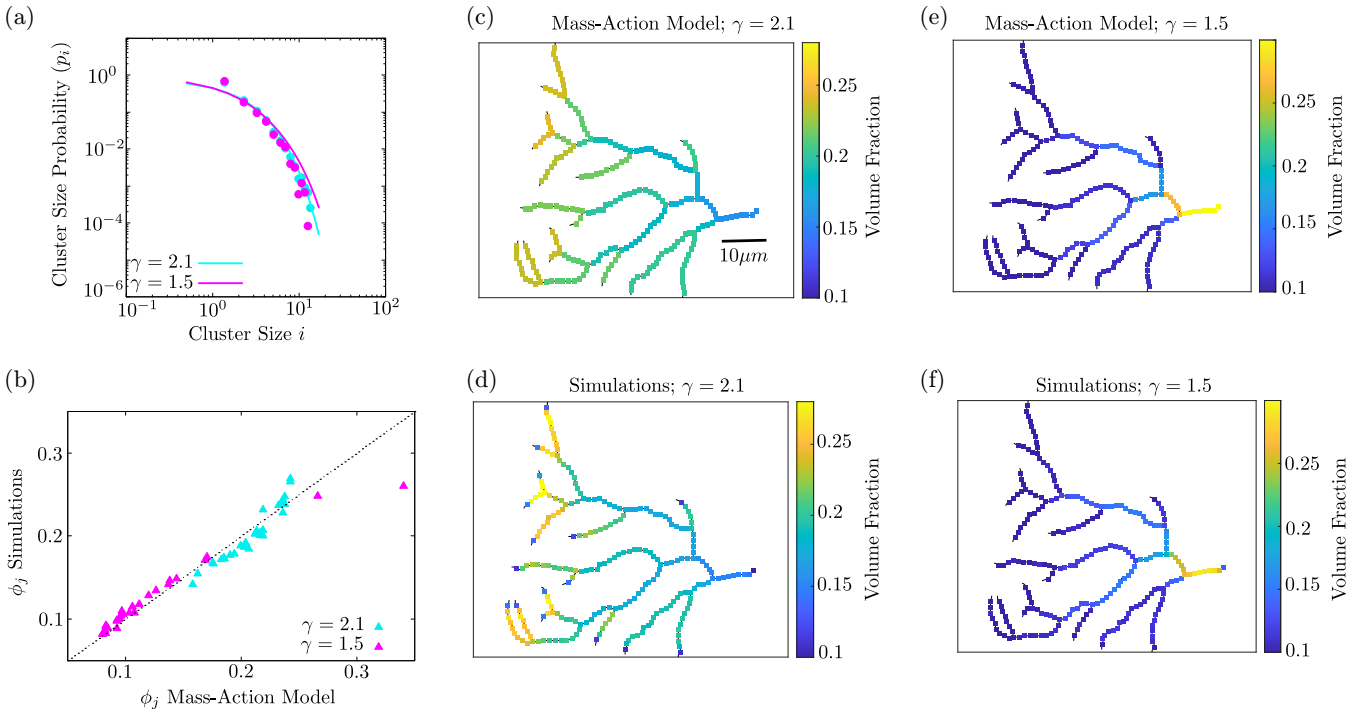

FIG. 2. Mass-action model and simulations of cluster distributions on a balanced tree structure. (a) Distribution of cluster sizes p_i averaged across the tree for $\gamma = 2.1$ (cyan) and $\gamma = 1.5$ (magenta); circles from simulation data and solid lines from Eq. (6). (b) Mitochondrial volume fraction on each branch ($\phi_j = \nu c_j$) is compared for simulations (horizontal axis) and mass-action model (vertical axis) for $\gamma = 2.1$ (cyan) and $\gamma = 1.5$ (magenta). Dashed line indicates equality. [(c) and (d)] Spatial distribution of mitochondrial volume fraction ϕ_j from (c) the mass-action model and (d) simulations, using $\gamma = 2.1$. [(e) and (f)] Analogous plots using $\gamma = 1.5$. Simulation parameters were $k_b = 0.01\ \mathrm{s}^{-1}$, $v = 0.6\ \mu\mathrm{m/s}$, trunk radius $r_0 = 1.3\ \mu\mathrm{m}$, with $A_u = \{0.05, 0.07\}$ and $k_p = \{0.34\ \mathrm{s}^{-1}, 0.32\ \mathrm{s}^{-1}\}$ selected to give average cluster size $\langle i \rangle = 2$ and overall volume fraction $\phi = 0.2$ in the mass-action model. Simulation results are averaged over 100 independent iterations.

volume fraction is $\phi = \nu \sum_j c_j \ell_j r_j^2 / \sum_j \ell_j r_j^2 \approx 20\%$ and the average cluster size is $\langle i \rangle_T = \sum_i i p_i \approx 2$, based on prior measurements in HS dendritic arbors [10].

The cluster size distribution exhibits an exponentially decaying tail, with a close match between simulations and the mass-action model [Fig. 2(a)]. The distributions are similar for different values of the scaling exponent γ, so long as the overall fusion rate (A_u) is adjusted to maintain the same average cluster size.

The predicted mitochondrial volume densities in individual branches are also similar for the mass-action model and the simulations [Fig. 2(b)]. Notably, a low value of γ results in more mitochondrial mass in the primary trunk [Figs. 2(e) and 2(f)], while a higher value yields distal enrichment of the mitochondrial density [Figs. 2(c) and 2(d)]. This is intuitively expected, as increasing γ raises the fusion rate in narrow distal branches relative to the wide primary trunk.

Unlike the mass-action model, the simulations show a depletion of mitochondrial densities at the terminal tips of the branches [Fig. 2(d)]. This effect arises from the finite size of mitochondrial units, which limits further fusion once a long cluster abuts the tip. For comparison with simulations, the mass-action model results are corrected to account for finite mitochondrial size which reduces the effective production rate of new mitochondria at the root node (see Appendix D for details). Nevertheless, the mass-action model encompasses the main features of the cluster size and spatial distributions in the simulated system.

B. Kinetic parameters and tree structure govern mitochondrial cluster distribution

We next determine how the total mitochondrial mass and its distribution into clusters emerges from the interplay of production, fusion/fission, and transport parameters, as well as the tree architecture. The kinetic parameters can be combined into a handful of intuitively interpretable dimensionless groups. The balance between new mitochondrial production and the time for motile units to traverse the tree is set by $\hat{k}_p = k_p D_0 / v$. Given that the rate at which a given mitochondrion undergoes fusion events must scale as $P_u v \rho$ (where ρ is the linear density of mitochondria along a branch), we define a dimensionless parameter governing the balance between fusion and fission as: $u = A_u v / (r_0^\gamma D_0 k_b)$. We note an analogy to prior models of binding and unbinding particles [38], with $\hat{k}_p$ serving as an effective fugacity (equivalent to the exponent of the chemical potential, driving more particles into the system) and u serving as an effective association constant (balancing the preference for clustering versus fragmentation). The current model extends these general concepts from equilibrium statistical mechanics to describe the steady state of a system of actively driven processive particles.

It can be shown (see Appendix E) that for any given tree structure, the linear densities of clusters ($m_{0,j}$) and of

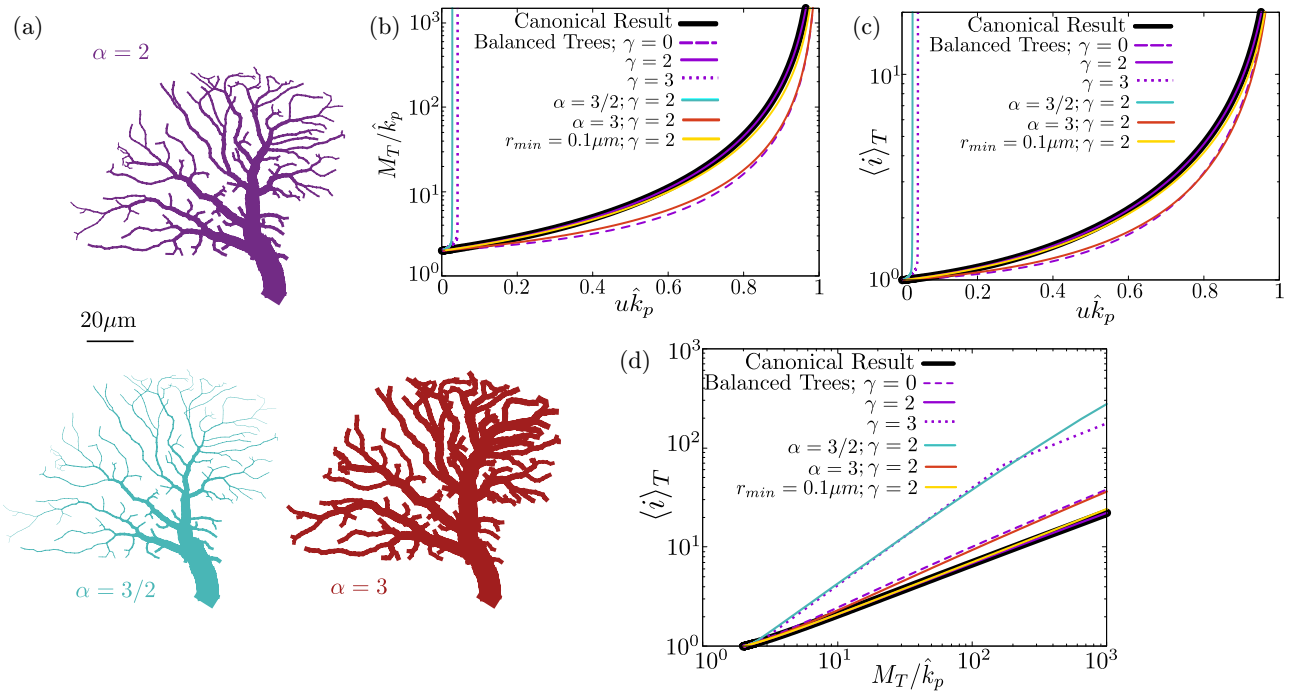

FIG. 3. Dependence of mitochondrial mass and cluster size on kinetic parameters and tree architecture from the mass-action model. (a) Example dendritic arbor from *Drosophila* HS neuron, with imposed radii following different scaling laws relating mother and daughter branches: $\alpha = 2, \frac{3}{2}, 3$. In all cases sister trunk radii are scaled in proportion to subtree bushiness: $r_k^2/r_l^2 = B_k/B_l$. (b) Scaled total mitochondrial mass plotted versus dimensionless parameter $u\hat{k}_p$, for different tree morphologies (α) and different fusion sensitivity scaling (γ). (c) Average cluster size plotted versus $u\hat{k}_p$. (d) Average cluster size plotted as a function of scaled mitochondrial mass. Black lines show canonical result on linear geometry with $\gamma = 2$. All other curves are computed on the example tree geometry in (a), with varying scaling laws for the radii. Purple lines show results for a balanced tree structure and different fusion scaling exponents: $\gamma = \{0, 2, 3\}$ (dashed, solid, and dotted curves respectively). Cyan and red curves represent alternate radial scaling laws ($\alpha = 3/2$ and $\alpha = 3$, respectively), with $\gamma = 2$. Yellow curves represent a balanced tree structure with an imposed minimum radius $r_{\min} = 0.1$ μm.

individual units ($m_{1,j}$) on each branch are given by:

$$m_{0,j} = \sum_{i=1}^{\infty} \rho_{i,j} = \frac{\xi_j \hat{k}_p}{D_0}\, g\left[u\hat{k}_p \xi_j \left(\frac{r_0}{r_j}\right)^{\gamma}\right],$$
$$m_{1,j} = \sum_{i=1}^{\infty} i\rho_{i,j} = \frac{\xi_j \hat{k}_p}{D_0}\, f\left[u\hat{k}_p \xi_j \left(\frac{r_0}{r_j}\right)^{\gamma}\right],$$
$$g(x) = 1 + \frac{1+x}{(1-x)}, \quad f(x) = 1 + \frac{1+x}{(1-x)^2}, \tag{8}$$

where $\xi_j = \rho^m_{1,j}/\rho^m_{1,0}$ describes how motile mitochondria are diluted as they travel downstream, completely determined by the branch widths of the tree. If the tree structure is fixed, then the scaled total mitochondrial mass, $M_T/\hat{k}_p = \frac{1}{\hat{k}_p}\sum_j m_{1,j}\ell_j$, is a function of the reduced parameter $u\hat{k}_p$ and the fusion sensitivity exponent γ [Fig. 3(b)]. Similarly, the average cluster size [Fig. 3(c)], given by $\langle i\rangle_T = (\sum_j m_{1,j}\ell_j)/(\sum_j m_{0,j}\ell_j)$, depends only on these two parameters and the tree structure. Unsurprisingly, increasing mitochondrial production (raising $\hat{k}_p$) increases both the size of the clusters formed and the total mass of mitochondria in the tree, with the latter rising in a superlinear manner, as expected for aggregating systems [29,33]. Furthermore, because larger clusters are immobile, increased fusion of mitochondria (raising u) causes each unit to spend more time in the tree before returning to the root, thereby raising the total mass.

For trees that obey the da Vinci law, the splitting of motile mitochondria in proportion to branch area implies that $\xi_j = (r_j/r_0)^2$. Consequently, in the case of $\gamma = 2$, the volume density of all cluster sizes is uniform across the tree. The average cluster size is then given by a universal curve:

$$\langle i\rangle_T = \frac{f(u\hat{k}_p)}{g(u\hat{k}_p)} = \frac{(u\hat{k}_p)^2 - u\hat{k}_p + 2}{2(1-u\hat{k}_p)}, \tag{9}$$

regardless of the tree connectivity (see Supplemental Fig. S1 [37]). The scaled total mitochondrial mass becomes

$$\frac{M_T}{\hat{k}_p} = \frac{f(u\hat{k}_p)V_T}{D_0 r_0^2} = \left[1 + \frac{1+u\hat{k}_p}{(1-u\hat{k}_p)^2}\right], \tag{10}$$

where V_T is the total volume of the tree. For the special case of balanced trees (where branch areas split in proportion to subtree bushiness), we have $V_T = \pi r_0^2 D_0$ and the scaled mass also becomes independent of the tree branching architecture. In particular, these universal expressions Eq. (9) and Eq. (10) [black curves in Figs. 3(b) and 3(c)] give the cluster size and the scaled mass for particles on a simple linear domain. They are analogous to the canonical behavior found in classic well-mixed mass aggregation models which exhibit a phase transition with increasing fusion or production [29,33]. Both

the total mass and cluster size diverge asymptotically when the parameter $u\hat{k}_p$ approaches a critical value, which for balanced trees is given by $(u\hat{k}_p)^* = (\min\{r_j\}/r_0)^{\gamma-2}$. Thus, when fusion probabilities scale with cross-sectional area ($\gamma = 2$), the critical value is $(u\hat{k}_p)^* = 1$, whereas for steeper fusion sensitivity ($\gamma > 2$), this critical value is lower [Figs. 3(b) and 3(c)].

We next consider the behavior of the total mass and average cluster size for alternate tree structures that obey distinct radial scaling laws. For instance, when the parent and daughter radii are related by $r_j^\alpha = r_k^\alpha + r_l^\alpha$ with $\alpha = 3/2$ (Rall's law [39]), the total cross-sectional area is reduced across each junction. In such trees, the fusion probability increases more steeply towards the distal tips, inducing the formation of larger distal clusters. The critical value $(u\hat{k}_p)^*$ for divergent mass and cluster size is then much lower, so that comparatively low production rates can lead to substantial accumulation of distal mitochondria. When $\alpha = 3$ (Murray's law [40]) the corresponding expansion of the cross-sectional area at the distal zone reduces the fusion probability and leads to smaller clusters for the same production rate.

In power-law models for tree structure, the cross-sectional area of the branches decreases exponentially from the primary trunk to the distal tips. However, there is likely a lower bound on the minimum radius of dendritic branches due to the mechanical limits of fitting at least one microtubule into each branch. Recent measurements in *Drosophila* class IV sensory neurons [41] indicate that the branch radii can be approximated as obeying a modified da Vinci relation: $r_1^2 + r_2^2 = r_0^2 + r_{\min}^2$, with minimum radius $r_{\min} \approx 0.1$ μm. We consider the effect of incorporating this minimum radius into the model for mitochondrial cluster formation on the *Drosophila* HS dendritic arbors considered here, which have an average radius of $r_{\text{trunk}} \approx 3$ μm in the primary trunk [10]. Imposing a balanced tree architecture yields an average radius of ∼0.3 μm in the distal branches. Consequently, the minimum radius has only a small effect in widening distal tree branches and reducing cluster size (Fig. 3).

In general, cells can adjust rates of mitochondrial biogenesis to control their overall mitochondrial load [42]. Thus, a fixed mitochondrial mass in the dendrite may be a more relevant control parameter than the production rate. In the regime where clusters of substantial size are formed ($\langle i\rangle_T \gtrsim 2$), a balanced tree architecture with fusion exponent $\gamma = 2$ yields the smallest average cluster sizes for a given total mass [Fig. 3(d)]. A variety of HS dendritic trees with different branch width scaling laws, $\alpha = \{3/2, 3\}$, all give larger clusters for a given scaled mitochondrial mass (see Supplemental Fig. S1 [37]). Thus, balanced trees with $\gamma \approx 2$ form the optimal structure to disperse the mitochondrial population into many small clusters, a direct consequence of the spatially uniform distributions that arise in such systems. These results highlight the importance of dendritic tree morphology in modulating the clustering and accumulation of actively driven particles.

C. Balanced trees allow for symmetric distributions with distally enriched large clusters

The spatial accumulation of mitochondria in different regions of the tree can be quantified by comparing clusters in distal branches versus the primary trunk [Fig. 4(a)]. We define the distal enrichment in volume density according to:

$$c_d/c_p = \left(\frac{\sum_{\text{distal } j} \rho_j \ell_j}{\sum_{\text{distal } j} \ell_j r_j^2}\right) \Big/ \left(\frac{\rho_0}{r_0^2}\right), \tag{11}$$

where the first term gives the total volume density in the set of distal branches (defined as those with path length from the root greater than 70% of the maximal value) and the second term gives the volume density in the primary trunk. Analogously, the cluster size ratio is defined as:

$$\langle i\rangle_d/\langle i\rangle_p = \left(\frac{\sum_{i=1}^{\infty}\sum_{\text{distal } j} i\rho_{i,j}\ell_j}{\sum_{i=1}^{\infty}\sum_{\text{distal } j}\rho_{i,j}\ell_j}\right) \Big/ \left(\frac{\sum_{i=1}^{\infty} i\rho_{i,0}}{\sum_{i=1}^{\infty}\rho_{i,0}}\right), \tag{12}$$

Focusing on balanced tree morphologies, these two quantities are plotted in Fig. 4(b) as a function of the fusion scaling exponent γ.

As previously noted, the scaling exponent $\gamma = 2$ gives uniform volume densities throughout the tree, so that $c_d/c_p = \langle i\rangle_d/\langle i\rangle_p = 1$. Higher values of γ enrich the mitochondrial volume in distal branches while lower values lead to enrichment in the proximal trunk, as also observed in simulations (Fig. 2). The ratio of distal to proximal cluster sizes also rises with increasing γ, albeit less steeply.

The twofold distal enrichment of volume density observed *in vivo* [10] is obtained with fusion sensitivity exponent $\gamma^* \approx 2.1$. For this parameter, the average cluster size is expected to be about 42% larger in distal versus proximal branches. Thus, enriching the mitochondrial mass in the distal tips of the arbor also requires increasing the size of clusters in that region. Notably, this is a concrete experimentally testable prediction of our model: distal enrichment in mitochondrial density is expected to be accompanied by larger clusters in the distal zone. The prediction could be tested by correlating individual mitochondrial volumes with their position in the dendritic arbor.

We note that the probability of two axially passing particles coming in direct contact scales as $1/r^2$ when the size of the particles is small compared to the tube width, but should exhibit a steeper scaling in narrow tubes comparable to the particle size [43]. Thus, values of $\gamma > 2$ are to be expected for narrow distal branches. Raising the overall fusion probability [Fig. 4(c)] monotonically amplifies the enrichment of mitochondria in either the distal or proximal zones, depending on the value of γ.

Finally, we consider the predicted asymmetry of the mitochondrial distribution in sister subtrees. Measurements in HS neurons have demonstrated that the average mitochondrial volume density in sister subtrees tends to be equal, even when the subtree morphologies themselves are asymmetric [10]. We define an asymmetry metric

$$\zeta = \sqrt{\frac{1}{N_b}\sum_b \left(\frac{c_{b,\text{ST1}} - c_{b,\text{ST2}}}{c_{b,\text{ST1}} + c_{b,\text{ST2}}}\right)^2}, \tag{13}$$

where b is a junction site, N_b is the total number of junctions in the tree, and $c_{b,\text{ST1/2}}$ are the average volume densities in the two subtrees emanating from the junction [Fig. 4(d)]. For balanced trees, perfectly symmetric distributions are predicted for $\gamma = 2$, with the asymmetry levels remaining quite low

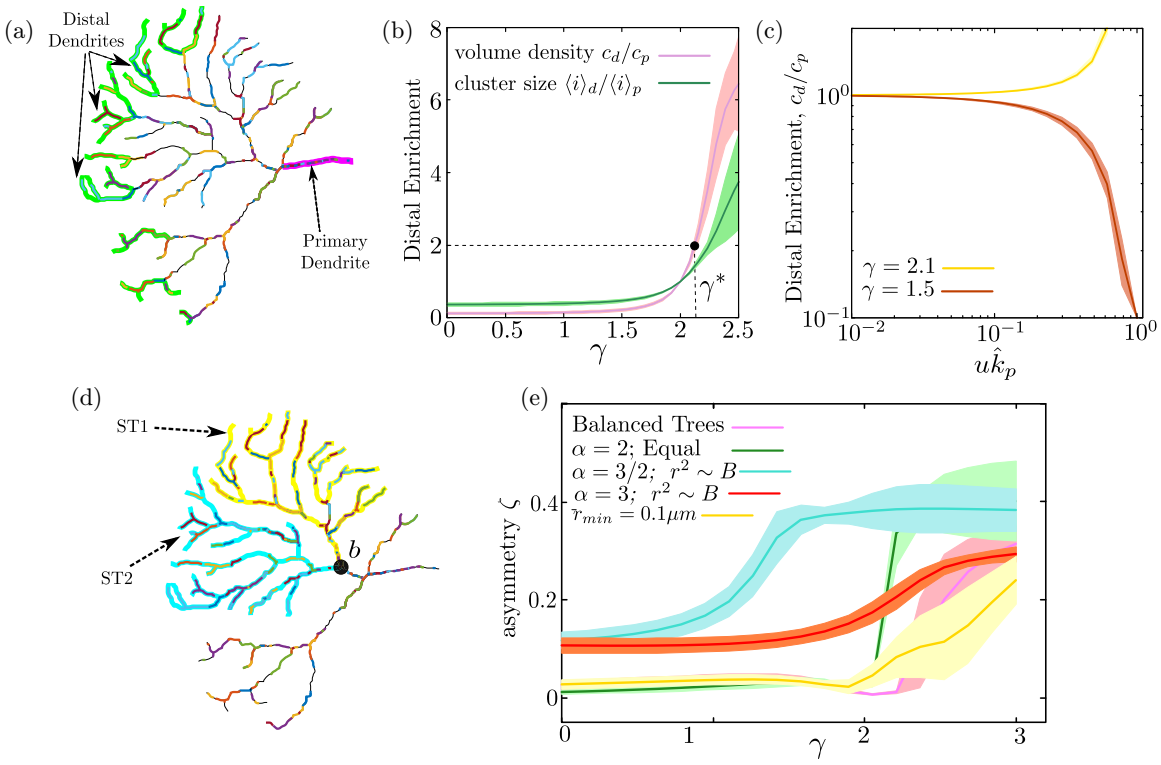

FIG. 4. Spatial distribution of mitochondral clusters. (a) Illustration of distal branches (green) and proximal trunk (magenta) in example dendritic arbor. Colored strokes show individual mitochondrial clusters from a simulation snapshot with $\gamma = 2.5$, $u\hat{k}_p = 0.18$; note larger clusters in the distal zone. (b) Distal-to-proximal ratio in volume density (pink) and average cluster size (green) plotted against fusion scaling exponent γ. Fusion and production parameters $(u, \hat{k}_p)$ are adjusted to give average cluster size $\langle i\rangle_T = 2$ and volume density $\phi = 0.2$ for the full tree. Experimentally observed distal enrichment (dashed line) corresponds to $\gamma^* = 2.1$. (c) Distal enrichment in volume density versus $u\hat{k}_p$ for $\gamma = \{1.5, 2.1\}$, with volume density fixed to $\phi = 0.2$. (d) Illustration of two sister subtrees, ST_1 (yellow) and ST_2 (cyan), at junction b in a sample dendritic arbor. (e) Root-mean-squared asymmetry (ζ) of mitochondrial volume density plotted against scaling exponent γ. Curves are shown for different radii scaling laws: $\alpha = 2, 3/2, 3$ (pink, cyan, and orange) with sister radii split in proportion to subtree bushiness, $\alpha = 2$ with equal sister radii (green), and balanced trees with imposed minimum radius $r_{\min} = 0.1$ μm (yellow). Average cluster size is fixed to $\langle i\rangle_T = 2$, volume density to $\phi \sim 0.2$. All results are obtained from the mass-action model, averaged over 10 tree topologies of distinct HS dendritic arbors (Supplemental Fig. S1 [37]); shadowed areas denote standard deviation.

over a broad range of γ values [Fig. 4(e)], extending past the $\gamma^* \approx 2.1$ approximation which gives twofold distal enrichment as observed *in vivo*. Notably, other tree morphologies, such as a tree that obeys the da Vinci law but has equal radii between sister branches (green curve), or trees with alternate scaling exponents α (blue, orange curves), lead to much higher asymmetry when $\gamma > 2$. The introduction of a minimum radius (yellow curve) also increases the asymmetry of the mitochondrial distribution for intermediate γ values. Overall, we show that a balanced tree morphology, approximately representative of HS dendrites, allows for a moderate amount of distal enrichment with a largely symmetric distribution of mitochondria.

The ability of balanced tree structures to maintain symmetric yet distally enriched mitochondrial distributions has previously been shown for a simpler model that does not include mitochondrial fusion into clusters but does allow for a width-dependent halting rate [10]. In that purely fragmented model, spatially uniform halting rates lead to uniform distribution of the mitochondria. When halting is attributed specifically to fusion, then spatially uniform fusion probabilities ($\gamma = 0$) result in proximal enrichment of the mitochondrial mass. Uniform distribution requires instead a fusion probability that scales inversely with cross-sectional area [$\gamma = 2$, Fig. 4(b)]. Furthermore, the presence of fusion results in very high sensitivity to increasing γ values above this value, as compared to the fragmented case. This effect can be observed in Fig. 4(c): As the fusion prefactor increases, the distal enrichment for two different γ values rapidly diverges. These results demonstrate that the ability of mitochondria to fuse into larger clusters exacerbates the sensitivity of the mitochondrial spatial distribution to the architecture of the dendritic arbor.

IV. DISCUSSION

Maintaining homeostasis of mitochondrial clusters in a neuronal arbor requires a balance of production, transport, fusion, and fission. The mass action model described here elucidates the key parameters which set the typical cluster size and overall mitochondrial accumulation: namely, the ratio of production and tree traversal rates ($\hat{k}_p$) and the ratio of fusion to fission (u). The tree morphology affects mitochondrial distributions through both regulating the

splitting of anterograde mitochondrial flux and modulating the probability of fusion between passing mitochondria (via the scaling exponent γ). Balanced trees architectures, which conserve branch area across junctions and split sister subtree trunk radii in proportion to bushiness, are shown to maintain a symmetric distribution of mitochondria among subtrees, while allowing for enrichment at the distal tips. Such enrichment goes hand-in-hand with larger clusters in the distal region.

The functional role of fusing dendritic mitochondria into larger clusters is not currently well understood. It is possible that such fusion can aid the mixing of mitochondrial contents, permitting the delivery of newly produced mitochondrial material from the cell body, and thereby maintaining the overall health of the population [9]. Alternately, mitochondrial fusion into larger structures has been proposed to enable complementation of damaged mitochondrial nucleoids [25], to protect healthy mitochondria from clearance through mitophagy [44], or to permit tunneling of ions through "power cables" [7].

Regardless of the specific advantages conveyed by modest fusion, there is a fundamental spatial constraint that makes hyperfusion of neuronal mitochondria detrimental to the cell. Namely, the need to broadly distribute mitochondria across extensive projections necessitates a finite mitochondrial population to be broken up into smaller clusters that can be spread throughout the dendritic arbor. In hippocampal dendrites, for example, it has been shown that ATP gradients form in dendrites when the spacing between mitochondria exceeds approximately 30 μm, limiting the energy supply for local translation [11]. In axons of the mammalian central nervous system, stationary mitochondria have been shown to distribute uniformly along the axonal length [45]. Furthermore, a sufficient population of motile mitochondria is necessary for maintenance and delivery of that fraction of mitochondrial proteins which is translated in the perinuclear zone [9,46]. Our results show that limiting the average cluster size is required to maintain such a motile population. Furthermore, we demonstrate that the balanced tree architecture previously observed in *Drosophila* HS neurons is optimized for dispersing mitochondria into the smallest clusters. Future work will explore the consequences of mitochondrial clustering and spatial distribution on the mixing of mitochondrial material throughout the arbor.

In the basic model considered here, mitochondrial transport and fusion is taken to be dependent only on the local width of the dendritic branch without any more sophisticated sensing and control mechanisms. The resulting mitochondrial distributions are found to be highly sensitive to small changes in domain geometry or in the production and fusion kinetics. The difficulty of controlling the size of cellular structures without direct length-sensing feedback mechanisms has previously been pointed out in the context of cytoskeletal filaments and flagellar projections [47]. For mitochondria, additional biochemical mechanisms have been found to regulate transport via the sensitivity of mitochondrial motor adaptors to local calcium [17] and glucose [16]. Intermitochondrial signaling via ATP gradients has also been proposed to regulate the mitochondrial distribution in axons [45]. Furthermore, mitochondrial fusion and fission may be regulated by local calcium concentrations [48]. It should be noted, however, that mitochondria in fly sensory dendrites were not found to respond to synaptic activity or altered calcium levels [10]. In general, additional levels of biochemical control could interplay with the basic "blind" transport and fusion/fission dynamics considered here, in a manner dependent on cell type and activity. By considering the simplest model for mitochondrial positioning, this work sheds light on some of the key physical parameters that can be tuned by the cell to alter the total volume, cluster architecture, and spatial distribution of the mitochondrial population that supplies the energetic needs of the dendritic arbor.

ACKNOWLEDGMENTS

We thank Erin Barnhart for helpful discussions. Support for this work was provided by the National Science Foundation, Grants No. 2310229 and No. 1848057.

APPENDIX A: SIMULATIONS OF MITOCHONDRIAL DYNAMICS IN DENDRITIC TREES

Stochastic simulations of mitochondrial transport, fusion, and fission were implemented on a network of one-dimensional edges. The network topology was taken from the dendritic arbor of a *Drosophila* HS neuron [10] [Fig. 1(a)], and a distal subtree was extracted for the simulations (Fig. 2).

The simulations were implemented in Fortran 90. For each run, 275 single mitochondrial units (corresponding to a mitochondrial volume fraction of $\phi = 0.2$) were placed on the subtree, with the number initialized on each branch proportional to the branch volume ($v_j = \pi l_j r_j^2$). Each mitochondrion was treated as a linear segment of length $\Delta x = 0.5$ μm. Each mitochondrion was initialized in a motile state, walking either in the anterograde (away from the root) or retrograde (towards the root) direction. At every time step $\Delta t = 0.01$s, motile mitochondria moved a distance of $\pm v\Delta t$ along the branch, with the speed set to $v = 0.6$ μm/s. Whenever an anterograde mitochondrion hit a terminal tip, it reversed and becomes retrograde until it reached the root, where it disappeared. Anterograde mitochondria split at junctions in proportion to daughter branch area πr_j^2. Aside from fusion, there was no interaction or exclusion between passing mitochondria.

The simulations were done for two different fusion exponents $\gamma = \{2.1, 1.5\}$, favoring the presence of high mitochondrial volume density at the distal zone ($\gamma = 2.1$) and primary trunk ($\gamma = 1.5$). In each case, new mitochondria were produced at the primary trunk with constant rates $k_p = \{0.34\ \mathrm{s}^{-1}, 0.32\ \mathrm{s}^{-1}\}$. When a motile mitochondrion passed the tip of any mitochondrial cluster (or another motile mitochondrion) fusion was allowed to occur with probability: $P_{u,j} = A_u/r_j^\gamma$, with $A_u = \{0.05, 0.07\}$ in the two different simulations. All clusters containing more than one unit were assumed to remain stationary.

For both fusion exponents, any cluster with size $i > 1$ could undergo fission and release a single motile unit, with fission rate $k_b = 0.01\ \mathrm{s}^{-1}$ from either end. Fission always produced one stationary unit or cluster plus one motile unit. A stationary mitochondrion of size $i = 1$ could become motile again with the same rate k_b in each direction. To achieve

the steady state configuration, the simulations were run for 10^8 steps.

APPENDIX B: STEADY-STATE SOLUTION

Here we solve Eq. (1) in the main text via recursive methods. Reflection of motile units at terminal tips implies that $\rho^+_{1,j} = \rho^-_{1,j}$ in the distal branches, and this equality propagates through boundary conditions at all junctions. Therefore, we can write the total linear density of motile monomers as $\rho^m_{1,j} = \rho^+_{1,j} + \rho^-_{1,j} = 2\rho^+_{1,j}$. The steady-state equations can then be re-expressed as:

$$\frac{\partial \rho^s_{1,j}}{\partial t} = -2k_b\rho^s_{1,j} + 2k_b\rho^s_{2,j} - vP_{u,j}\rho^m_{1,j}\rho^s_{1,j} = 0, \tag{B1a}$$

$$\frac{\partial \rho^m_{1,j}}{\partial t} = -vP_{u,j}\rho^m_{1,j}\sum_{i=1}^{\infty}\rho^s_{i,j} - vP_{u,j}\left(\rho^m_{1,j}\right)^2 + 2k_b\sum_{i=1}^{\infty}\rho^s_{i,j} = 0, \tag{B1b}$$

$$\frac{\partial \rho^s_{2,j}}{\partial t} = -vP_{u,j}\rho^m_{1,j}\rho^s_{2,j} + vP_{u,j}\frac{\left(\rho^m_{1,j}\right)^2}{2} + 2k_b\rho^s_{3,j} - 2k_b\rho^s_{2,j} + vP_{u,j}\rho^m_{1,j}\rho^s_{1,j} = 0, \tag{B1c}$$

$$\frac{\partial \rho^s_{i,j}}{\partial t} = vP_{u,j}\rho^m_{1,j}\left(\rho^s_{i-1,j} - \rho^s_{i,j}\right) + 2k_b\rho^s_{i+1,j} - 2k_b\rho^s_{i,j} = 0. \tag{B1d}$$

Solving Eq. (B1c) gives an expression for $\rho^s_{3,j}$ as:

$$\rho^s_{3,j} = \rho^s_{2,j} + \left(\rho^s_{2,j} - \rho^s_{1,j} - \frac{\rho^m_{1,j}}{2}\right)\alpha_j\rho^m_{1,j}, \tag{B2}$$

where we define $\alpha_j = vP_{u,j}/(2k_b) = vA_u/(2k_br_j^\gamma)$. Solving Eq. (B1d) for $\rho^s_{i+1,j}$ and propagating downward recursively gives a general expression for the linear density of all clusters of size $i > 2$:

$$\rho^s_{i,j} = \rho^s_{2,j} + \left(\rho^s_{2,j} - \rho^s_{1,j} - \frac{\rho^m_{1,j}}{2}\right)\sum_{k=1}^{i-2}\left(\alpha_j\rho^m_{1,j}\right)^k. \tag{B3}$$

Assuming $|\alpha_j\rho^m_{i,j}| < 1$, we can explicitly sum the partial geometric series to get:

$$\rho^s_{i,j} = \frac{1}{1-\alpha_j\rho^m_{i,j}}\left[\rho^s_{2,j} - \alpha_j\rho^m_{1,j}\left(\rho^s_{1,j} + \frac{\rho^m_{1,j}}{2}\right) - \left(\alpha_j\rho^m_{1,j}\right)^{i-1}\left(\rho^s_{2,j} - \rho^s_{1,j} - \frac{\rho^m_{1,j}}{2}\right)\right]. \tag{B4}$$

For a finite total mitochondrial load, the density must vanish at large cluster sizes: $\lim_{i\to\infty}\rho^s_{i,j} = 0$. This implies that the intercept in Eq. (B4) must be zero:

$$\rho^s_{2,j} = \alpha_j\rho^m_{1,j}\left(\rho^s_{1,j} + \frac{\rho^m_{1,j}}{2}\right). \tag{B5}$$

Solving Eq. (B1a) then gives:

$$\rho^s_{2,j} = \rho^s_{1,j} + \alpha_j\rho^m_{1,j}\rho^s_{1,j}. \tag{B6}$$

Together, Eqs. (B4), (B5), and (B6) give the full solution for the steady-state density of stationary clusters as a function of the motile density: Equation (2) in the main text.

The motile density in each branch is found by applying the boundary condition at the root ($\rho^m_{1,0} = 2k_p/v$) and the continuity and anterograde splitting conditions at each junction:

$$\rho^m_{1,j} = \rho^m_{1,k} + \rho^m_{1,l}, \quad \frac{\rho^m_{1,k}}{\rho^m_{1,l}} = \frac{r_k^2}{r_l^2}. \tag{B7}$$

APPENDIX C: DEFINITION OF TREE DEPTH

The depth of a subtree starting with parent branch j is defined recursively, as in Eq. (5) in main text, via the following relation:

$$D_j = \ell_j + \frac{L_k + L_l}{L_k/D_k + L_l/D_l}, \tag{C1}$$

where L_k is the total branch length in the daughter subtree stemming from branch k, and D_k is the depth of that subtree. We note that for a subtree consisting of a single branch, or one where all branch tips are the same path length from the root, the depth is equal to that path length. For more complicated tree structures, this recursive definition involves an average of inverse depth for the daughter subtrees, weighted by the total branch length in that tree.

For balanced tree structures, this definition of depth is closely related to the volume of the entire tree. Balanced trees are defined as preserving area across junctions: $r_j^2 = r_k^2 + r_l^2$, as well as splitting sister branch areas in proportion to the bushiness of the supported subtrees: $r_k^2/r_l^2 = B_k/B_l$. For such trees, the ratio of daughter (k) to parent(j) branch area is given by:

$$\frac{r_k^2}{r_j^2} = \frac{L_k/D_k}{L_k/D_k + L_l/D_l}. \tag{C2}$$

Suppose that the total tree volume for the subtree stemming from branch k is given by $V_k = \pi r_k^2 D_k$. This is trivially true for a subtree composed of a single branch, where $D_k = \ell_k$. We then proceed by induction to show that this relation holds for all balanced tree structures. For a parent branch j with daughters k, l, we can use Eq. (C2) to simplify the volume of the subtree beginning from j:

$$\begin{aligned} V_j &= \pi r_j^2\ell_j + V_k + V_l = \pi r_j^2\ell_j + \pi r_k^2 D_k + \pi r_l^2 D_l, \\ &= \pi r_j^2\left(\ell_j + \frac{r_k^2}{r_j^2}D_k + \frac{r_l^2}{r_j^2}D_l\right), \\ &= \pi r_j^2\left(\ell_j + \frac{L_k}{L_k/D_k + L_l/D_l} + \frac{L_l}{L_k/D_k + L_l/D_l}\right), \\ &= \pi r_j^2 D_j. \end{aligned} \tag{C3}$$

Thus, the volume of the entire tree can also be expressed as $V_0 = r_0^2 D_0$. This simple relationship motivates our recursive definition for the tree depth. The depth is defined based on branch lengths only, matches the trivial definition for simple trees where all tips are at the same distance from the root, and

has an intuitively clear relationship with the tree volume and trunk width for an area-preserving balanced tree.

APPENDIX D: CORRECTION FOR FINITE MITOCHONDRIAL LENGTH

When comparing mean-field results to simulations (Fig. 2), we include an additional correction to account for the finite length of mitochondria ($\Delta x = 0.5$ μm in simulations). Specifically, whenever a new mitochondrion is produced, it extends a distance Δx into the primary trunk and has a chance to fuse into existing clusters immediately. The overall rate at which produced mitochondria disappear due to immediate fusion at the root is $vP_{u,0}\rho^+_{1,0}m_{0,0}\Delta x$, where $m_{0,0}$ is the total linear density of all clusters at the root, and $\rho^+_{1,0}\Delta x$ describes the number of anterograde mitochondria at the root. Consequently, we adjust the boundary condition at the tree root such that the rate of new mitochondria produced (k_p) is equal to the rate at which such new mitochondria move into the primary branch ($v\rho^+_{1,0}$) plus the rate at which they vanish due to immediate fusion:

$$k_p = v\rho^+_{1,0} + vP_{u,0}\rho^+_{1,0}m_{0,0}\Delta x. \tag{D1}$$

We use this alternate boundary condition to solve for the motile mitochondria in the primary trunk ($\rho^m_{1,0} = 2\rho^+_{1,0}$). Putting together Eqs. (8) and (D1), gives a quadratic expression for this motile density:

$$\left\{\alpha_0 k_b \Delta x - \frac{v\alpha_0}{2}\right\}\left(\rho^m_{1,0}\right)^2 + \left\{\frac{v}{2} + \alpha_0 k_p\right\}\rho^m_{1,0} - k_p = 0, \tag{D2}$$

where $\alpha_0 = vP_{u,0}/2k_b$. The solution of Eq. (D2) is then used as the motile density in the primary trunk, with all other motile densities obtained through Eq. (4).

When Δx is much smaller than the branch lengths of the tree, this reduces to the standard solution for point particles as given in the main text. For simplicity, we use the point-particle model without finite-length correction throughout the main text, other than in the simulation comparison in Fig. 2.

APPENDIX E: MOMENTS AND AVERAGES OF THE DISTRIBUTION

The overall linear density of mitochondrial clusters on branch j is given by summing Eq. (2) over all cluster sizes:

$$\begin{aligned} m_{0,j} &= \rho^m_{1,j} + \sum_{i=1}^{\infty}\rho^s_{i,j}, \\ &= \frac{\rho^m_{1,j}}{2} + \frac{\rho^m_{1,j}\left(1+\alpha_j\rho^m_{1,j}\right)}{2\left(1-\alpha_j\rho^m_{1,j}\right)}. \end{aligned} \tag{E1}$$

Similarly, the linear density of individual mitochondrial units is given by the next moment of the distribution:

$$\begin{aligned} m_{1,j} &= \rho^m_{1,j} + \sum_{i=1}^{\infty} i\rho^s_{i,j}, \\ &= \frac{\rho^m_{1,j}}{2} + \frac{\rho^m_{1,j}\left(1+\alpha_j\rho^m_{1,j}\right)}{2\left(1-\alpha_j\rho^m_{1,j}\right)^2}, \end{aligned} \tag{E2}$$

We define the dilution factor $\xi_j = \rho^m_{1,j}/\rho^m_{1,0}$, which depends only on the tree structure (specifically, on the radii of all branches upstream of j). Additionally, we define the two dimensionless quantities $\hat{k}_p = \frac{k_p D_0}{v}$, and $u = \frac{A_u v}{r_0^\gamma D_0 k_b}$, where D_0 is the depth of the tree. This yields the following expressions:

$$\begin{aligned} \rho^m_{1,j} &= \xi_j\rho^m_{1,0} = \xi_j(2k_p/v) = 2\xi_j\hat{k}_p/D_0, \\ \alpha_j\rho^m_{1,j} &= vA_u/\left(2k_b r_j^\gamma\right) \times 2\xi_j\hat{k}_p/D_0 = \xi_j u\hat{k}_p r_0^\gamma/r_j^\gamma. \end{aligned} \tag{E3}$$

Equations (E1), (E2), and (E3) yield Eq. (8) in the main text. The above moments of the mitochondrial cluster distribution can be used to compute total mass, volume density, and average cluster size in different tree regions.

The total mitochondrial mass in tree T is given by

$$M_T = \sum_{j\in T} m_{1,j}\ell_j, \tag{E4}$$

where ℓ_j is the length of the jth branch. The average cluster size is defined as the ratio of the total mitochondrial mass divided by the total number of clusters in the tree:

$$\langle i\rangle_T = M_T/\sum_{j\in T} m_{0,j}\ell_j. \tag{E5}$$

The mitochondrial volume density in a a given branch is given by $c_j = m_{1,j}/(\pi r_j^2)$. The average mitochondrial volume density over a tree or subtree (T) is defined as the total mass divided by the tree volume:

$$c_T = M_T/V_T = \frac{M_T}{\sum_{j\in T}\pi\ell_j r_j^2}. \tag{E6}$$

APPENDIX F: CANONICAL SOLUTION FOR $\gamma = 2$ ON BALANCED TREES

We next consider the mitochondrial distribution on specialized tree structures. A tree obeys da Vinci's law if the cross-sectional area is conserved across all junctions ($r_j^2 = r_k^2 + r_l^2$, for parent branch j and daughter branches k, l). For such trees, Eq. (3) implies that $\xi_j = r_j^2/r_0^2$. If we further assume that the fusion sensitivity exponent is set to $\gamma = 2$, the moments of the mitochondrial distribution [Eq. (8)] can be simplified to

$$\begin{aligned} m_{0,j} &= \frac{r_j^2\hat{k}_p}{r_0^2 D_0} g[u\hat{k}_p], \\ m_{1,j} &= \frac{r_j^2\hat{k}_p}{r_0^2 D_0} f[u\hat{k}_p]. \end{aligned} \tag{F1}$$

As a result, the average cluster size [Eq. (E5)] is given by

$$\langle i\rangle_{T,\text{daVinci}} = \frac{f[u\hat{k}_p]}{g[u\hat{k}_p]} = \frac{(u\hat{k}_p)^2 - u\hat{k}_p + 2}{2(1-u\hat{k}_p)}. \tag{F2}$$

Thus, for da Vinci trees, the average cluster size is independent of the tree topology or the specific choice of branch radii.

A balanced tree structure is one that both obeys da Vinci's law and splits sister branches such that cross-sectional area is proportional to the bushiness of the two subtrees which they support ($r_k^2/r_l^2 = B_k/B_l$ at each junction, where $B_k = L_k/D_k$ is the length divided by the depth of the subtree stemming from branch k). The relation of depth and volume in balanced trees [Eq. (C3)] allows a simple universal expression for the total mitochondrial mass in a balanced tree (when $\gamma = 2$). Combining Eqs. (E4), (F1), and (C3) yields

$$M_{T,\text{balanced}} = \hat{k}_p f[u\hat{k}_p]\frac{\sum_j r_j^2 \ell_j}{V_0},$$
$$= \hat{k}_p f[u\hat{k}_p] = \hat{k}_p\left[1 + \frac{1 + u\hat{k}_p}{(1 - u\hat{k}_p)^2}\right]. \quad \text{(F3)}$$

[1] M. P. Viana, A. I. Brown, I. A. Mueller, C. Goul, E. F. Koslover, and S. M. Rafelski, Mitochondrial fission and fusion dynamics generate efficient, robust, and evenly distributed network topologies in budding yeast cells, Cell Syst. **10**, 287 (2020).

[2] J. Faitg, C. Lacefield, T. Davey, K. White, R. Laws, S. Kosmidis, A. K. Reeve, E. R. Kandel, A. E. Vincent, and M. Picard, 3D neuronal mitochondrial morphology in axons, dendrites, and somata of the aging mouse hippocampus, Cell Rep. **36**, 109509 (2021).

[3] A. D. Pilling, D. Horiuchi, C. M. Lively, and W. M. Saxton, Kinesin-1 and dynein are the primary motors for fast transport of mitochondria in drosophila motor axons, Mol. Biol. Cell **17**, 2057 (2006).

[4] V. M. Sukhorukov, D. Dikov, A. S. Reichert, and M. Meyer-Hermann, Emergence of the mitochondrial reticulum from fission and fusion dynamics, PLOS Comput. Biol. **8**, e1002745 (2012).

[5] N. Zamponi, E. Zamponi, S. A. Cannas, O. V. Billoni, P. R. Helguera, and D. R. Chialvo, Mitochondrial network complexity emerges from fission/fusion dynamics, Sci. Rep. **8**, 363 (2018).

[6] K. B. Holt, J. Winter, S. Manley, and E. F. Koslover, Spatiotemporal modeling of mitochondrial network architecture, PRX Life **2**, 043002 (2024).

[7] H. Hoitzing, I. G. Johnston, and N. S. Jones, What is the function of mitochondrial networks? A theoretical assessment of hypotheses and proposal for future research, BioEssays **37**, 687 (2015).

[8] M. Picard and C. Sandi, The social nature of mitochondria: Implications for human health, Neurosci. Biobehav. Rev. **120**, 595 (2021).

[9] A. Agrawal and E. F. Koslover, Optimizing mitochondrial maintenance in extended neuronal projections, PLOS Comput. Biol. **17**, e1009073 (2021).

[10] E. J. Donovan, A. Agrawal, N. Liberman, J. I. Kalai, A. J. Adler, A. M. Lamper, H. Q. Wang, N. J. Chua, E. F. Koslover, and E. L. Barnhart, Dendrite architecture determines mitochondrial distribution patterns in vivo, Cell Rep. **43**, 114190 (2024).

[11] V. Rangaraju, M. Lauterbach, and E. M. Schuman, Spatially stable mitochondrial compartments fuel local translation during plasticity, Cell **176**, 73 (2019).

[12] M.-H. Schuler, A. Lewandowska, G. D. Caprio, W. Skillern, S. Upadhyayula, T. Kirchhausen, J. M. Shaw, and B. Cunniff, Miro1-mediated mitochondrial positioning shapes intracellular energy gradients required for cell migration, Mol. Biol. Cell **28**, 2159 (2017).

[13] V. S. Van Laar and S. B. Berman, Mitochondrial dynamics in Parkinson's disease, Exp. Neurol. **218**, 247 (2009).

[14] E. A. Schon and S. Przedborski, Mitochondria: The next (neurode) generation, Neuron **70**, 1033 (2011).

[15] A. Mandal and C. M. Drerup, Axonal transport and mitochondrial function in neurons, Front. Cell. Neurosci. **13**, 373 (2019).

[16] G. Pekkurnaz, J. C. Trinidad, X. Wang, D. Kong, and T. L. Schwarz, Glucose regulates mitochondrial motility via milton modification by O-GlcNAc transferase, Cell **158**, 54 (2014).

[17] X. Wang and T. L. Schwarz, The mechanism of Ca^{2+}-dependent regulation of kinesin-mediated mitochondrial motility, Cell **136**, 163 (2009).

[18] A. F. MacAskill and J. T. Kittler, Control of mitochondrial transport and localization in neurons, Trends Cell Biol. **20**, 102 (2010).

[19] D. M. Virga, S. Hamilton, B. Osei, A. Morgan, P. Kneis, E. Zamponi, N. J. Park, V. L. Hewitt, D. Zhang, K. C. Gonzalez *et al.*, Activity-dependent compartmentalization of dendritic mitochondria morphology through local regulation of fusion-fission balance in neurons in vivo, Nat. Commun. **15**, 2142 (2024).

[20] J. P. Richter *et al.*, *The Notebooks of Leonardo da Vinci* (Dover Publications, Inc., Minneola, New York, 1970), Vol. 2.

[21] S. Mai, M. Klinkenberg, G. Auburger, J. Bereiter-Hahn, and M. Jendrach, Decreased expression of Drp1 and Fis1 mediates mitochondrial elongation in senescent cells and enhances resistance to oxidative stress through PINK1, J. Cell Sci. **123**, 917 (2010).

[22] R. J. Youle and A. M. van der Bliek, Mitochondrial fission, fusion, and stress, Science **337**, 1062 (2012).

[23] M. Liesa and O. S. Shirihai, Mitochondrial dynamics in the regulation of nutrient utilization and energy expenditure, Cell Metab. **17**, 491 (2013).

[24] B. Westermann, Mitochondrial fusion and fission in cell life and death, Nat. Rev. Mol. Cell Bio. **11**, 872 (2010).

[25] D. A. Knorre, Intracellular quality control of mitochondrial DNA: evidence and limitations, Phil. Trans. R. Soc. B **375**, 20190176 (2020).

[26] A. Kowald and T. B. Kirkwood, Evolution of the mitochondrial fusion—fission cycle and its role in aging, Proc. Natl. Acad. Sci. USA **108**, 10237 (2011).

[27] J. Aryaman, I. G. Johnston, and N. S. Jones, Mitochondrial heterogeneity, Front. Genet. **9**, 718 (2019).

[28] B. R. J. Narayanareddy, S. Vartiainen, N. Hariri, D. K. O'Dowd, and S. P. Gross, A biophysical analysis of mitochondrial movement: Differences between transport in neuronal cell bodies versus processes, Traffic **15**, 762 (2014).

[29] Z. Budrikis, G. Costantini, C. A. La Porta, and S. Zapperi, Protein accumulation in the endoplasmic reticulum as a

non-equilibrium phase transition, Nat. Commun. **5**, 3620 (2014).
[30] T. P. Knowles, C. A. Waudby, G. L. Devlin, S. I. Cohen, A. Aguzzi, M. Vendruscolo, E. M. Terentjev, M. E. Welland, and C. M. Dobson, An analytical solution to the kinetics of breakable filament assembly, Science **326**, 1533 (2009).
[31] R. M. Ziff, Kinetics of polymerization, J. Stat. Phys. **23**, 241 (1980).
[32] P. Blatz and A. Tobolsky, Note on the kinetics of systems manifesting simultaneous polymerization-depolymerization phenomena, J. Phys. Chem. **49**, 77 (1945).
[33] H. Takayasu, I. Nishikawa, and H. Tasaki, Power-law mass distribution of aggregation systems with injection, Phys. Rev. A **37**, 3110 (1988).
[34] S. N. Majumdar, S. Krishnamurthy, and M. Barma, Nonequilibrium phase transitions in models of aggregation, adsorption, and dissociation, Phys. Rev. Lett. **81**, 3691 (1998).
[35] P. L. Krapivsky and E. Ben-Naim, Aggregation with multiple conservation laws, Phys. Rev. E **53**, 291 (1996).
[36] P. L. Krapivsky, S. Redner, and E. Ben-Naim, *A Kinetic View of Statistical Physics* (Cambridge University Press, Cambridge, UK, 2010).
[37] See Supplemental Material at http://link.aps.org/supplemental/10.1103/PhysRevResearch.6.043312 for Supplemental Fig. S1 and Video SV1.
[38] F. M. Weinert, R. C. Brewster, M. Rydenfelt, R. Phillips, and W. K. Kegel, Scaling of gene expression with transcription-factor fugacity, Phys. Rev. Lett. **113**, 258101 (2014).
[39] W. Rall, Branching dendritic trees and motoneuron membrane resistivity, Exp. Neurol. **1**, 491 (1959).
[40] C. D. Murray, The physiological principle of minimum work applied to the angle of branching of arteries, J. Gen. Physiol. **9**, 835 (1926).
[41] M. Liao, X. Liang, and J. Howard, The narrowing of dendrite branches across nodes follows a well-defined scaling law, Proc. Natl. Acad. Sci. USA **118**, e2022395118 (2021).
[42] I. G. Onyango, J. Lu, M. Rodova, E. Lezi, A. B. Crafter, and R. H. Swerdlow, Regulation of neuron mitochondrial biogenesis and relevance to brain health, BBA-Mol Basis Dis, BBA-Mol. Basis Dis. **1802**, 228 (2010).
[43] S. S. Mogre, J. R. Christensen, C. S. Niman, S. L. Reck-Peterson, and E. F. Koslover, Hitching a ride: Mechanics of transport initiation through linker-mediated hitchhiking, Biophys. J. **118**, 1357 (2020).
[44] A. S. Rambold, B. Kostelecky, N. Elia, and J. Lippincott-Schwartz, Tubular network formation protects mitochon- dria from autophagosomal degradation during nutrient starvation, Proc. Natl. Acad. Sci. USA **108**, 10190 (2011).
[45] N. Matsumoto, I. Hori, M. K. Kajita, T. Murase, W. Nakamura, T. Tsuji, S. Miyake, M. Inatani, and Y. Konishi, Intermitochondrial signaling regulates the uniform distribution of stationary mitochondria in axons, Mol. Cell Neurosci. **119**, 103704 (2022).
[46] S.-K. Lee and P. J. Hollenbeck, Organization and translation of mRNA in sympathetic axons, J. Cell Sci. **116**, 4467 (2003).
[47] L. Mohapatra, B. L. Goode, P. Jelenkovic, R. Phillips, and J. Kondev, Design principles of length control of cytoskeletal structures, Annu. Rev. Biophys. **45**, 85 (2016).
[48] D. V. Jeyaraju, G. Cisbani, and L. Pellegrini, Calcium regulation of mitochondria motility and morphology, Biochim. Biophys. Acta Bioenerg. **1787**, 1363 (2009).